JGR Space Physics

RESEARCH ARTICLE
10.1029/2019JA026821

Properties of Magnetic Reconnection and FTEs on the Dayside Magnetopause With and Without Positive IMF B_x Component During Southward IMF

S. Hoilijoki[1,2], U. Ganse[2], D. G. Sibeck[3], P. A. Cassak[4], L. Turc[2], M. Battarbee[2], R. C. Fear[5], X. Blanco-Cano[6], A. P. Dimmock[7,8], E. K. J. Kilpua[2], R. Jarvinen[7,9], L. Juusola[2,9], Y. Pfau-Kempf[2], and M. Palmroth[2,9]

[1]Laboratory for Atmospheric and Space Physics, University of Colorado Boulder, Boulder, CO, USA, [2]Department of Physics, University of Helsinki, Helsinki, Finland, [3]NASA Goddard Space Flight Center, Greenbelt, MD, USA, [4]Department of Physics and Astronomy, West Virginia University, Morgantown, WV, USA, [5]Department of Physics and Astronomy, University of Southampton, Southampton, UK, [6]Instituto de Geofisica, Universidad Nacional Autonoma de Mexico, Mexico City, Mexico, [7]Department of Electronics and Nanoengineering, School of Electrical Engineering, Aalto University, Espoo, Finland, [8]Swedish Institute of Space Physics, Uppsala, Sweden, [9]Finnish Meteorological Institute, Helsinki, Finland

Key Points:
- Sunward IMF tilt results in a smaller tangential field at the magnetopause, slowing dayside reconnection
- Smaller tangential field results from a decrease in the IMF component that is shocked up at the bow shock
- A positive IMF B_x component introduces north-south asymmetries, where fewer (but larger) FTEs appear on the Southern Hemisphere

Supporting Information:
- Supporting Information S1
- Movie S1

Correspondence to:
S. Hoilijoki,
sanni.hoilijoki@lasp.colorado.edu

Citation:
Hoilijoki, S., Ganse, U., Sibeck, D. G., Cassak, P. A., Turc, L., Battarbee, M., et al. (2019). Properties of magnetic reconnection and FTEs on the dayside magnetopause with and without positive IMF B_x component during southward IMF. *Journal of Geophysical Research: Space Physics*, *124*, 4037–4048. https://doi.org/10.1029/2019JA026821

Received 10 APR 2019
Accepted 22 APR 2019
Accepted article online 1 MAY 2019
Published online 6 JUN 2019

©2019. American Geophysical Union. All Rights Reserved.

Abstract This paper describes properties and behavior of magnetic reconnection and flux transfer events (FTEs) on the dayside magnetopause using the global hybrid-Vlasov code Vlasiator. We investigate two simulation runs with and without a sunward (positive) B_x component of the interplanetary magnetic field (IMF) when the IMF is southward. The runs are two-dimensional in real space in the noon-midnight meridional (polar) plane and three-dimensional in velocity space. Solar wind input parameters are identical in the two simulations with the exception that the IMF is purely southward in one but tilted 45° toward the Sun in the other. In the purely southward case (i.e., without B_x) the magnitude of the magnetosheath magnetic field component tangential to the magnetopause is larger than in the run with a sunward tilt. This is because the shock normal is perpendicular to the IMF at the equatorial plane, whereas in the other run the shock configuration is oblique and a smaller fraction of the total IMF strength is compressed at the shock crossing. Hence, the measured average and maximum reconnection rate are larger in the purely southward run. The run with tilted IMF also exhibits a north-south asymmetry in the tangential magnetic field caused by the different angle between the IMF and the bow shock normal north and south of the equator. Greater north-south asymmetries are seen in the FTE occurrence rate, size, and velocity as well; FTEs moving toward the Southern Hemisphere are larger in size and observed less frequently than FTEs in the Northern Hemisphere.

1. Introduction

The solar wind-magnetosphere coupling drives the dynamic evolution of Earth's magnetosphere. Phenomena at the dayside magnetopause associated with the coupling impact the entire magnetosphere, including the radiation belts and the magnetotail (e.g., Baker et al., 1996; Burton et al., 1975; McPherron et al., 1986). Magnetic reconnection represents the most significant component of the coupling (e.g., Dungey, 1961), which is strongest when the interplanetary magnetic field (IMF) is southward (e.g., Akasofu, 1981). Consequently, it is important to understand how the nature of reconnection on the magnetopause varies as a function of solar wind conditions.

Before interacting with the magnetic field of Earth, the solar wind first passes through the bow shock and then propagates through the magnetosheath. Reconnection at the dayside magnetopause connects magnetosheath magnetic fields to magnetospheric fields. Simplified sketches of dayside reconnection often invoke a single quasi-steady reconnection site (e.g., Dungey, 1961), but observations suggest that dayside reconnection is often bursty, giving rise to FTEs (Russell & Elphic, 1978), which are commonly observed at the dayside magnetopause (e.g., Fear et al., 2007, 2012; Kawano & Russell, 1997; Rijnbeek et al., 1984; Wang et al., 2006). Statistical surveys find that FTEs form quasiperiodically, on average once every 8 min (Rijnbeek et al., 1984). Reconnection may occur at single (Fedder et al., 2002; Southwood et al., 1988) or at multiple

reconnection (or X) lines (e.g., Lee & Fu, 1985). In the former case, the onset of reconnection results in bubble-like magnetic structures (e.g., Southwood et al., 1988) and in the latter case in flux ropes of interconnected magnetosheath and magnetospheric magnetic field lines (e.g., Lee & Fu, 1985). The scale sizes for FTE flux rope diameters can reach 1–2 R_E (e.g., Fear et al., 2007; Rijnbeek et al., 1984), while dimensions along the X line can be considerably longer (e.g., Fear et al., 2008). Recently, with the high-resolution observations provided by the Magnetospheric Multiscale mission (Burch et al., 2016) many smaller ion-scale flux rope structures have been observed (e.g., Dong et al., 2017; Eastwood et al., 2016; Zhong et al., 2018).

The north/south IMF B_z component is an important parameter controlling the overall reconnection rate (e.g., Vasyliunas, 1975), and it also impacts the formation and properties of the FTEs (e.g., Berchem & Russell, 1984; Rijnbeek et al., 1984; Wang et al., 2006). Berchem and Russell (1984) analyzed 5 years of ISEE (International Sun-Earth Explorer) observations and found that FTEs on the dayside tend to occur during southward IMF with only a few FTEs observed during slightly northward IMF. Wang et al. (2006) used 3 years of Cluster observations to show that IMF B_z impacts the peak-to-peak magnitudes (measured as the absolute difference between the bipolar peaks in the magnetic field component B_N normal to the magnetopause) and separation time between consecutive FTEs, with the separation time growing with increasing IMF B_z. For the present study, we focus on the orientation of the IMF when it has a negative (southward) B_z component.

Other factors may also control the nature and effectiveness of reconnection and FTEs on the dayside magnetopause. Both observations and simulations have been used to study the effects of the IMF clock angle, $\theta = \arctan(B_y/B_z)$, where B_y/B_z is the ratio between the IMF y (opposite Earth's motion around the Sun) and z (normal to the ecliptic) components, on the distribution of FTEs and the location of X lines (e.g., Fear et al., 2012; Karlson et al., 1996; Kawano & Russell, 1997). However, the influence of the sunward B_x component on FTE formation has not been as thoroughly investigated. Wang et al. (2006) reported that B_x controls the occurrence of FTEs but not the separation time or peak-to-peak magnitude of FTEs. They reported that more FTEs were observed during positive than negative IMF B_x. A statistical study using Time History of Events and Macroscale Interactions during Substorms (THEMIS) mission (Angelopoulos, 2008) observations and studies using global magnetohydrodynamic (MHD) simulations show that the X line shifts northward for sunward directed B_x and southward for antisunward B_x (Hoilijoki et al., 2014; Hoshi et al., 2018; Peng et al., 2010).

This study employs the hybrid-Vlasov code Vlasiator for the global magnetosphere (Palmroth et al., 2018; von Alfthan et al., 2014; http://www.helsinki.fi/vlasiator). In the present paper simulations are global and two-dimensional in real space and three-dimensional in velocity space (2D-3V). For simplicity, we consider systems without a dipole tilt and with steady solar wind conditions. We compare simulation results for two cases with the same total magnetic field strength but with different IMF tilt. In the first simulation the IMF is purely southward, and in the second simulation the IMF is tilted sunward by 45°. We find that the average reconnection rate is lower in the run with the sunward IMF B_x component due to the smaller tangential magnetic field magnitude in the magnetosheath. The tilt in the IMF direction also introduces north-south asymmetries in the observed properties of the FTEs, including occurrence rate, sizes of the FTEs, and their velocities.

This paper is organized as follows. The details of the simulations and their setup are presented in section 2. The data analysis and results are shown in section 3. Finally, we discuss the results and provide concluding remarks in section 4.

2. Simulation Setup

The simulations employ the Vlasiator global magnetospheric hybrid-Vlasov code (Palmroth et al., 2015, 2018; von Alfthan et al., 2014), where ions evolve as distribution functions in three velocity-space dimensions and electrons are treated as a massless fluid described by the generalized Ohm's law including the Hall term. The simulations are two-dimensional in ordinary space and confined to the noon-midnight meridional plane. The simulation using a purely southward IMF condition, referred to as Run A, is the same simulation discussed by Hoilijoki et al. (2017), Palmroth et al. (2017), Jarvinen et al. (2018), and Juusola et al. (2018), with a domain extending from −94 to +48 R_E in the x direction and from −56 to 56 R_E in the z direction, where R_E is Earth's radius, and we use geocentric solar ecliptic coordinates in which x points sunward, y points opposite Earth's motion about the Sun, and z points normal to the ecliptic plane. The simulation with

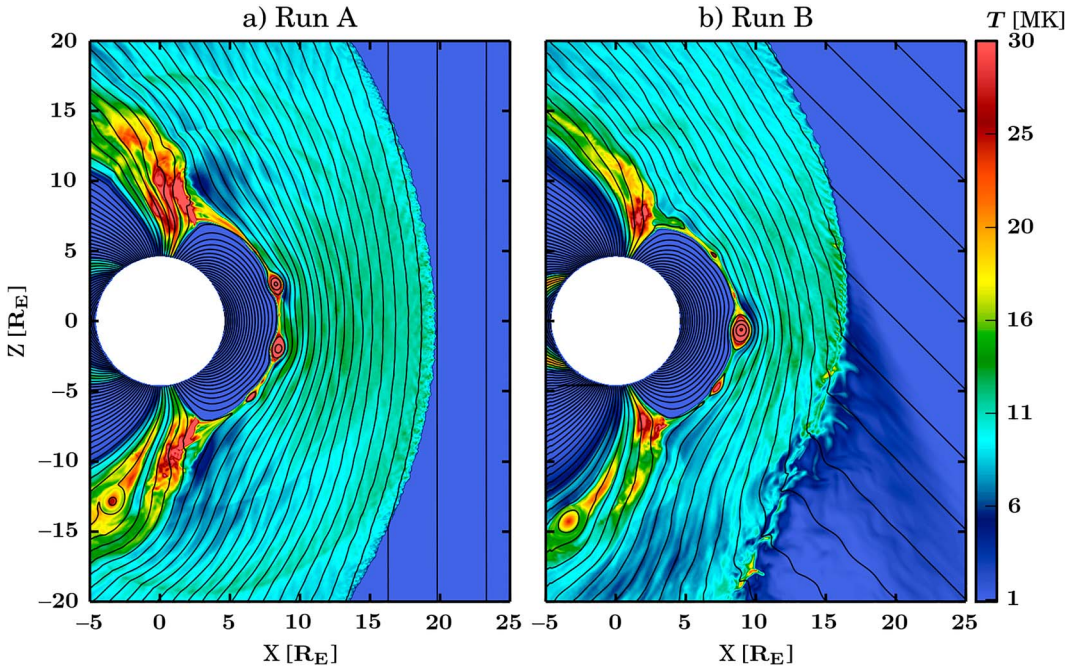

Figure 1. Overview plot showing the ion temperature with magnetic field lines overlaid for (a) Run A, the purely southward IMF simulation, and (b) Run B, the southward IMF with 45° sunward tilt. The time plotted is $t = 1,200$ s for both simulations.

a sunward tilted IMF, referred as Run B, has the same initial conditions except that the IMF is tilted sunward by 45° so that the magnitudes of the x and z components of the magnetic field are equal. The simulation domain for Run B spans −48 to +64 R_E in x and −59 to 39 R_E in the z direction to accommodate the foreshock that forms upstream from the south part of the bow shock. Run B produces cavitons and spontaneous hot flow anomalies in the foreshock, which are analyzed in a separate study (Blanco-Cano et al., 2018).

Solar wind parameters at the sunward boundary in x are held steady, including a fast solar wind with velocity of −750 km/s in the x direction, a density of $n = 1$ cm^{-3}, a proton temperature of $T_p = 0.5$ MK with a Maxwellian distribution, and a magnetic field of magnitude 5 nT, meaning that in Run A the magnetic field components are $B_x = 0$ and $B_z = -5$ nT and in Run B they are $B_x = 3.54$ nT and $B_z = -3.54$ nT. We point out that the goal of this study is to investigate the fundamental properties of FTEs and reconnection at the dayside magnetopause, so we do not attempt to simulate a magnetosphere with commonly observed properties; we do not believe that the results of this study are adversely impacted by the chosen solar wind parameters. The other three outer boundaries of the simulation domain apply a copy condition, that is, the magnetic field and the velocity distribution function are copied from the closest simulation spatial cells to the boundary cell allowing a smooth outflow. The out-of-plane direction has a periodic boundary condition. The inner boundary with a radius of $5R_E$ is an ideal conducting sphere. The grid resolution is 300 km in ordinary space and 30 km/s in velocity space.

Run A is carried out for $t = 2,150$ s of simulation time, while Run B is carried out for $t = 1,437$ s. The simulations are initialized slightly differently. Initially, both simulations set the solar wind density and velocity throughout the whole simulation domain and employ a 2-D line dipole with a strength resulting in a magnetopause standoff distance comparable to that of Earth's dipole, with a corresponding mirror dipole outside the solar wind inflow boundary. Details on the line dipole approach were described by Daldorff et al. (2014). The difference is that in Run A, the only magnetic field component initially in the simulation domain is that of the dipole field, while the IMF enters from the inflow boundary and pushes the dipole field to form the magnetosphere. In Run B, in addition to the dipole field, the IMF is also initially set throughout the whole simulation domain to preserve the solenoidality of the magnetic field in the presence of a nonzero IMF B_x component. Therefore, the reconnection at the dayside magnetopause becomes properly initialized earlier in Run B than in Run A; this does not impact the results of the study. We analyze the time period from 1,250 to 1,975 s for Run A and from 900 to 1,437 s for Run B.

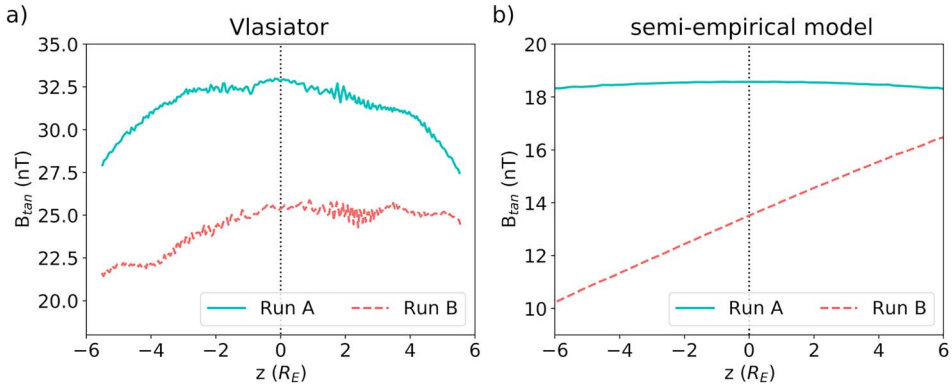

Figure 2. Average magnitude of the tangential magnetic field component from a distance of 3 R_E from the magnetopause from (a) Vlasiator simulations and (b) a semiempirical model based on magnetohydrodynamic.

3. Results

During the steady solar wind conditions, multiple FTEs occur in both Runs A and B as can be seen in Movie S1 in the supporting information. Figure 1 shows a sample time slice ($t = 1,200$ s) of the structure of the dayside magnetosphere and magnetosheath for each simulation. Here the color indicates that the ion temperature and magnetic field lines are overlaid so that the magnetic flux interval between consecutive magnetic field lines is the same in both panels. Figures 1a and 1b show, respectively, Run A (purely southward IMF simulation) and Run B (the simulation with sunward IMF tilt). In these simulations with only two spatial dimensions, FTEs appear in the form of closed magnetic islands. In Figure 1a the two largest FTEs are located at $x = 8\,R_E$ and $z = \pm 3\,R_E$ and in Figure 1b one large FTE is visible at $x = 9\,R_E$, $z = -1\,R_E$. Both simulations also exhibit a number of smaller FTEs with a range of sizes, including some too small to see in Figure 1.

3.1. Bow Shock Location and Tangential Magnetic Field

In both simulations, for the chosen strength of the line dipole moment, the equatorial dayside magnetopause lies approximately at 8 R_E from Earth. In Run A the bow shock is symmetric and extends up to 19 R_E from Earth on the dayside. Run B, with the IMF tilted toward the Sun, has a north-south asymmetry in the bow shock shape due to the foreshock and quasi-parallel bow shock in the south, while the nose of the bow shock lies at 16 R_E. The extent of the quasi-perpendicular magnetosheath becomes larger than the quasi-parallel, which is consistent with theory and previous findings (e.g., Chapman & Cairns, 2003; Lin et al., 1996; Turc et al., 2015). According to the Merka et al. (2005) bow shock model for the same upstream conditions as used in the simulation runs, Earth's subsolar bow shock is predicted to be located approximately at 15 R_E in both cases. The larger standoff distance of the bow shock in the simulations compared to the model is caused by the two-dimensionality of the simulation domain as the magnetic field and plasma can flow around the Earth only in the simulation plane and, therefore, pile on the dayside magnetosheath. However, the large extent of the magnetosheath in the simulation does not affect the local physics that occur at the bow shock, in the magnetosheath, and at the magnetopause. Vlasiator simulations have been found to reproduce observed features of the foreshock velocity distributions and waves (Kempf et al., 2015; Palmroth et al., 2015; Pfau-Kempf et al., 2016; Turc et al., 2018), foreshock transients (Blanco-Cano et al., 2018), magnetosheath mirror mode waves (Hoilijoki et al., 2016) and high-speed jets (Palmroth et al., 2018), and reconnection rates at the dayside magnetopause (Hoilijoki et al., 2017).

The magnetic field lines plotted in Figure 1 demonstrate that the magnetic field magnitude in the magnetosheath is smaller in Run B than in Run A. Figure 2a shows the average value of the magnitude of the magnetic field component tangential to the magnetopause B_{tan} measured at a distance of 3 R_E further outward into the magnetosheath to avoid the impact of the passing FTEs on the magnetic field. In Run A, B_{tan} is relatively symmetric between the Northern and Southern Hemispheres, and at the subsolar point the magnitude is almost 7 nT larger than in Run B. On the contrary, in Run B B_{tan} is larger in the Northern Hemisphere than in the southern one.

For comparison, we estimate the magnetosheath magnetic field component tangential to the magnetopause at the same distance from this boundary as in Vlasiator using a semiempirical model of the magnetosheath

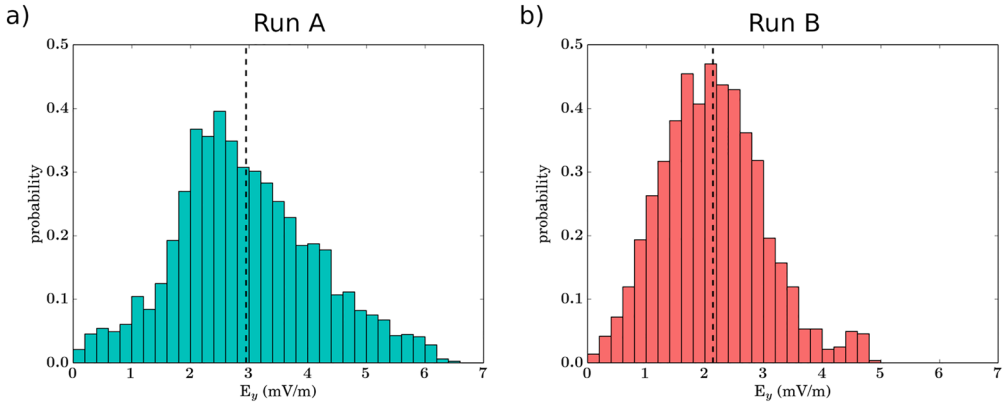

Figure 3. Normalized distribution of the reconnection rate E_y at X lines located between $z = \pm 4\ R_E$ and the mean reconnection rate (dashed line) in (a) Run A with mean at 2.9 mV/m and (b) Run B with mean at 2.1 mV/m.

magnetic field based on ideal MHD (Turc et al., 2014) shown in Figure 2b. We use as inputs to the model the upstream conditions of the two Vlasiator runs. The magnetic field just downstream of the bow shock is computed based on Rankine-Hugoniot relations, and it is then propagated into the magnetosheath using ideal MHD equations. A full description of the model is given by Turc et al. (2014). While the model initially employed the Jeřáb et al. (2005) bow shock model to estimate the position and shape of this boundary, because it was more reliable for the low Mach number conditions under study in Turc et al. (2014), we use here the Merka et al. (2005) bow shock model, better suited to the upstream conditions in the Vlasiator simulations. Also, as in Turc et al. (2017), the magnetic field compression ratio is calculated using the Borovsky (2013) formula. The behavior of the tangential magnetic field component given by the semiempirical model is similar to that in Vlasiator. In the purely southward case B_{tan} is largest at the equatorial plane and symmetric between north and south, whereas in the tilted IMF case B_{tan} is smaller and asymmetric increasing from south to north. Due to the magnetic field pileup caused by the two-dimensionality of the simulations, the magnitude of B_{tan} in Vlasiator simulations is larger than that given by the semiempirical model.

In Run A, the IMF is southward so that at the subsolar point the angle θ_{Bn} between the IMF and bow shock normal is 90°, that is, the shock is perpendicular and the magnetic field compression at the bow shock is highest. At higher latitudes, θ_{Bn} decreases, meaning that the IMF component normal to the bow shock increases, but the change is symmetric between the north and south. The magnetic field component normal to the shock is conserved in the shock crossing and only the tangential component is compressed (e.g., Treumann, 2009). Therefore, the tangential magnetic field in the magnetosheath diminishes at higher latitudes. Because of the sunward tilt in the IMF in Run B, the bow shock is quasi-parallel to the south and quasi-perpendicular to the north of the equator. At the equatorial plane $\theta_{Bn} = 45°$, only the IMF B_z component is compressed. Consequently, the magnetosheath magnetic field is weaker than in Run A. Also, in the Southern Hemisphere in the quasi-parallel magnetosheath the tangential magnetic field is smaller than in the Northern Hemisphere behind the quasi-perpendicular bow shock where a larger fraction of the IMF is compressed. Therefore, our simulations show that, despite the IMF draping around the magnetopause, the tilt in the IMF orientation causes differences in the magnitude of the magnetosheath magnetic field. This is important because the tangential component of the magnetic field is the component that participates in magnetic reconnection at the magnetopause.

3.2. Reconnection Rates

Using the method of flux functions described in Appendix A, we locate magnetic field X and O points that represent the reconnection points and the centers of magnetic islands (i.e., 2-D representations of FTEs), respectively. At each X point, we measure the reconnection rate as the out-of-plane component of the electric field E_y. Figure 3 shows the probability distributions of reconnection rates at X lines located between $z = \pm 4\ R_E$ from both simulations. The distribution of the reconnection rates in Run A is broader and reaches higher reconnection rates (above 6 mV/m). The average reconnection rate is 2.9 ± 1.2 mV/m (dashed line in Figure 3a), and the median is 2.8 mV/m. In Run B, the peak is steeper and the maximum reconnection rate is lower ($\sim$ 5 mV/m) than in Run A. Both the average and median values of the reconnection rate are 2.1 ± 0.9 mV/m in Run B (dashed line in Figure 3b).

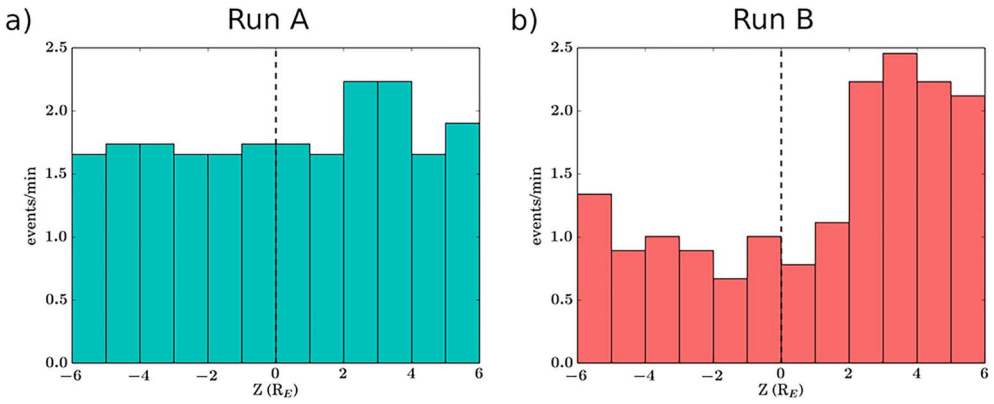

Figure 4. Distribution of number of flux transfer events observed in 1 minute within one 1 R_E bins along the dayside magnetopause in (a) Run A and (b) Run B. The horizontal axis shows the z coordinate along the magnetopause. The vertical dotted line in both panel depicts the equatorial plane.

The smaller reconnection rate in Run B is a consequence of the smaller tangential magnetic field in magnetosheath caused by the sunward IMF component discussed above. To see this, note that for θ_{Bn}, the southward component of the field is $1/\sqrt{2} \approx 0.707$ as big as it is for the due southward IMF case. The reconnection rate scales approximately as $[B_{sh}^{3/2} B_{\rm ms}/(B_{\rm sh} + B_{\rm ms})^{1/2}]/\sqrt{\mu_0 \rho_{\rm sh}}$ (Cassak & Shay, 2007), where $B_{\rm sh}$ and $B_{\rm ms}$ are the magnetosheath and magnetosphere reconnecting magnetic field strengths, $\rho_{\rm sh}$ is the magnetosheath density, and the magnetospheric density is assumed to be negligible. Using $B_{\rm ms} \simeq 60$ nT and $B_{\rm sh}$ decreasing from 32.5 to 25 nT, one finds that the reconnection rate decreases to approximately 70% of its due southward value. Note that 70% of 2.9 mV/m is 2.04 mV/m, in excellent agreement with the measured value of 2.1 mV/m. This suggests that the decrease in reconnection rate is due to the decrease in the strength of the reconnecting component of the magnetosheath magnetic field.

3.3. North-South Asymmetry of FTEs

Next, we study the probability of encountering an individual FTE at different locations along the dayside magnetopause. In order to do so, we need to identify the locations of each X point and O point (regarded as the centers of FTEs) at every time step, which we do using the flux function method described in Appendix A. Figures 4a and 4b illustrate the distribution of FTEs passing each point on the magnetopause (divided into 1 R_E bins) per minute from Run A and Run B, respectively. In Run A the FTE occurrence rate in both hemispheres and in the subsolar region is quite flat at ~1.7 FTEs/min (except for a small peak at $z \sim +3\,R_E$), and therefore, the chance of encountering FTEs does not depend on the hemisphere. In Run B, however, the rate of FTE encounters in the Northern Hemisphere is twice as large as in the Southern Hemisphere. This shows that the IMF B_x component causes a north-south asymmetry in the occurrence rate of FTEs.

It is also interesting to see if the sunward tilt in the IMF has an impact on FTE sizes and their evolution versus latitude. We calculate the enclosed area of the FTEs using the method described in Appendix B. Figure 5 shows the z coordinate of the FTE locations on the magnetopause plotted as a function of time for both simulations. The color and the area of the circle marking the location of each FTE are proportional to the cross-sectional area enclosed by the last closed field line of the FTE. The results show that the size of most of the FTEs increases as they move to higher latitudes. Some of the FTEs in Run A reach a cross-sectional area of $5R_E^2$ both north and south of the equator. These are the ones that spend longer times near the subsolar region before traveling poleward (Ku & Sibeck, 1998). There is a clear north-south asymmetry in the FTE enclosed area for Run B compared to Run A. In particular, the FTEs propagating northward in Run B remain relatively small, whereas in the south there are fewer FTEs, but two of them reach an enclosed area over $4.5R_E^2$, larger than is typical in Run A.

Figure 6a presents the dependence of FTE size on FTE location. Using the calculated enclosed area of each FTE and assuming a circular cross section, we estimate the average radius of the FTEs and plot it as a function of z coordinate in Figure 6a. In Run A, the average radius of the FTEs is close to ~1,500 km $\approx 10\,d_i$ (ion inertial length $d_i \approx 150$ km in the magnetosheath in the vicinity of the magnetopause in this simulation) near to the subsolar region. The region of smaller radius FTEs ($r < 2,000$ km), that is, the region where

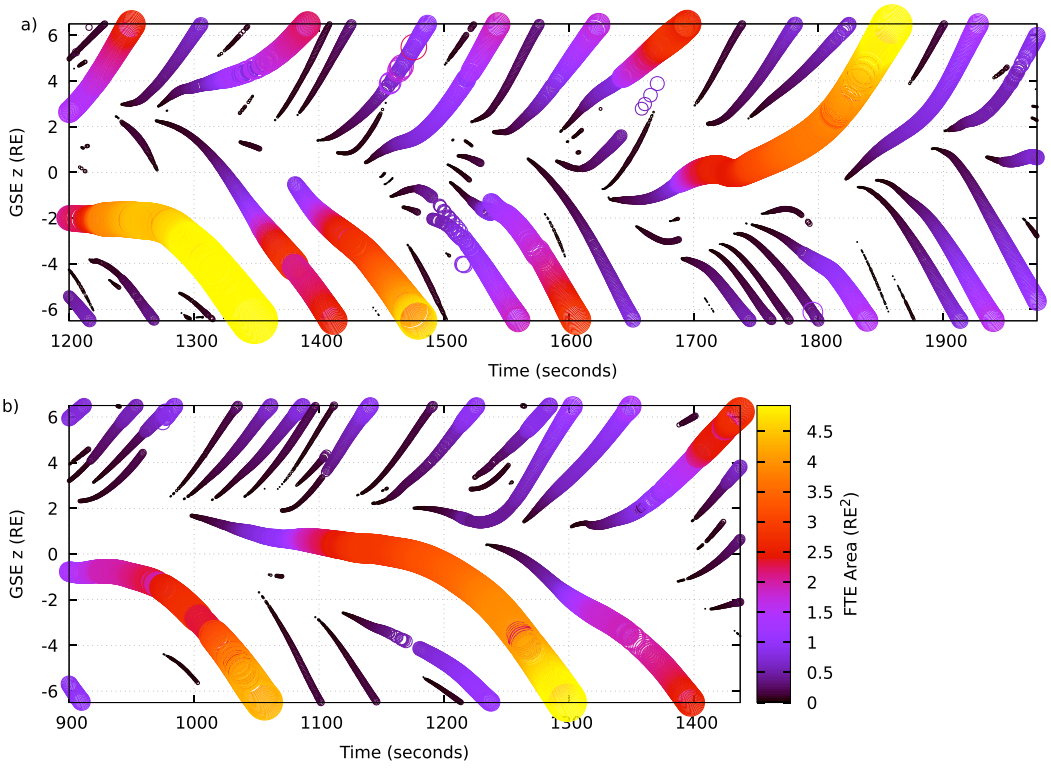

Figure 5. Location of the FTEs, color coded with the enclosed area. The area of the circles is proportional to the area of the closed field lines in (a) Run A and (b) Run B. GSE = geocentric solar ecliptic; FTE = flux transfer event.

they are generated, is slightly shifted northward from the subsolar region, residing between $z = -1\,R_E$ and $3\,R_E$. The average radius both in the Southern and Northern Hemispheres approaches ~2,750 km ($\approx 18\,d_i$) at higher latitudes. The FTEs keep growing after formation due to ongoing reconnection at the X lines encompassing the FTE. In the simulations FTE sizes also increase as they coalesce with other FTEs (e.g., Akhavan-Tafti et al., 2018; Finn & Kaw, 1977; Hoilijoki et al., 2017; Omidi et al., 2006). The FTE sizes exhibit more north-south asymmetry in Run B. The region where the FTEs are generated and their radius is small lies between $z = 1\,R_E$ and $4\,R_E$. On average the FTEs in the Southern Hemisphere grow larger than in the Northern Hemisphere because they form north of the equator and travel further along the magnetopause and therefore have a longer time to process flux through reconnection and coalesce with other FTEs. Statistical spacecraft studies have also shown that the FTEs observed near the subsolar region, which have an average radius of $15\,d_i$, are 3 to 7 times smaller than FTEs observed at higher latitudes (Akhavan-Tafti et al., 2018; Fermo et al., 2011; Wang et al., 2005). Our results suggest that the FTE radius roughly doubles from $\sim 10\,d_i$ in the subsolar region to almost $\sim 20\,d_i$ around $z = 7R_E$, which is consistent with the observations.

We calculate FTE velocities as the first-order time derivative of the O point locations as they propagate along the magnetopause. The results are plotted for both IMF cases averaged over $1\,R_E$ bins in the z direction in Figure 6b. In Run A (shown in cyan boxes), the profile of the average FTE velocities is broadly symmetric in both hemispheres. In Run B (shown in red circles), the FTEs propagating toward the northern cusp have larger velocities than those moving southward. FTEs propagate along the magnetopause as solid bodies having the same velocity as the plasma bulk velocity at the core of the FTEs. We suggest that as FTEs north of the equator are smaller, containing also less plasma, they require less force to accelerate to higher velocities than the larger FTEs on the Southern Hemisphere. In addition, the FTEs with the purely southward IMF are generally faster at the same latitude than the FTEs in the simulation with positive IMF B_x. It is possible that in Run A the faster outflow reconnection jet velocities that are caused by higher tangential magnetic field, $v_{\mathrm{out},2} \sim 0.84 v_{\mathrm{out},1}$ (Cassak & Shay, 2007), push the FTEs, and cause them to accelerate faster to higher velocities.

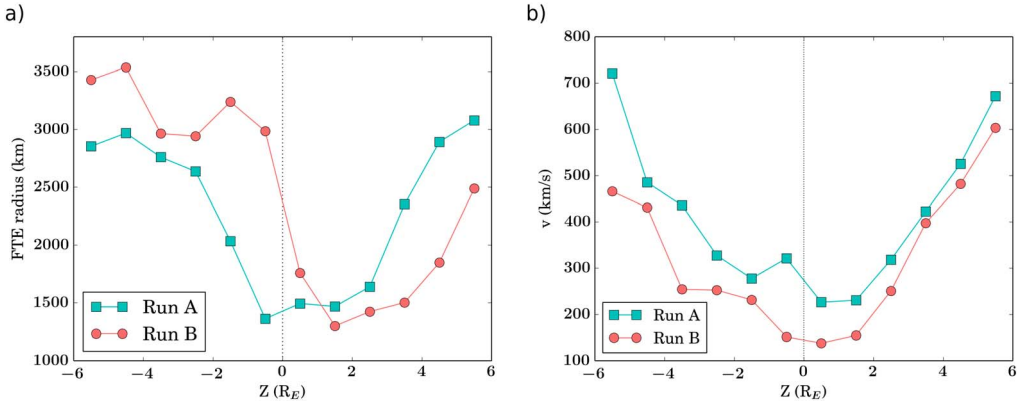

Figure 6. (a) Average radius of the FTEs at different points along the magnetopause as a function of z. (b) Average velocity of the FTEs as a function of z from both runs. The vertical dashed line depicts the equator. FTE = flux transfer event.

4. Discussion and Conclusions

This study describes properties of dayside magnetopause reconnection and FTEs in two global hybrid-Vlasov Vlasiator simulations. The only difference in the solar wind input values used for the two simulations is the orientation of the IMF. Run A has a purely southward IMF, whereas Run B has an IMF tilted 45° sunward, so that the magnitude of the southward B_z component is smaller and B_x is nonzero and positive. We find that even though the magnitude of the IMF is the same in both simulations, the magnetic field tangential to the magnetopause measured in the magnetosheath is smaller and has a north-south asymmetry in the simulation with sunward IMF component. These are caused by the different angle between the shock normal and IMF θ_{Bn}. When $\theta_{Bn} = 90°$, the IMF is strictly perpendicular to the bow shock and the magnetic field compression is highest at the shock crossing, which is the case at the nose of the bow shock in Run A with purely southward IMF. In Run B, with tilted IMF, the IMF component tangential to the bow shock is larger in the north and smaller in the south causing a north-south asymmetry in the magnetic field magnitude downstream of the shock. Because the dayside reconnection rate depends on the local tangential magnetic field (e.g., Cassak & Shay, 2007), the estimated reconnection rates at the X line locations on the dayside magnetopause in Run A exhibit a higher maximum and average rate than in Run B.

Some of the existing coupling functions that determine the reconnection rate at the magnetopause as a function of solar wind parameters include the effects of the clock angle between **B** and the z axis in the yz plane (e.g., Borovsky, 2013) but not the effect of the oblique θ_{Bn} in the xz plane that could cause a significant north-south asymmetry in the tangential magnetic field close to the magnetopause. A reconnection rate value calculated for the θ_{Bn} at the subsolar point or using only the IMF B_z component might not give an accurate description of the reconnection rate at an X line that is located north or south from the equator, suggesting that the effect of the sunward tilt needs to be incorporated at all latitudes to accurately predict the reconnection rates.

The north-south asymmetries introduced by the sunward tilt of the IMF suggest that the X line resides north of the equatorial plane for a longer period of time than in the strictly southward IMF run. The shift of the X line toward the Northern Hemisphere with positive IMF B_x component has been observed before in a statistical THEMIS study (Hoshi et al., 2018) and global MHD simulations (Hoilijoki et al., 2014; Peng et al., 2010). Often the shift of the X line is explained using the maximum magnetic shear model (Trattner et al., 2007, 2012), but in this case without an out-of-plane magnetic field B_y component the shear is the same everywhere along the magnetopause and, therefore, cannot explain the shift. A model based on maximization of a reconnection related parameter that is dependent on $B_{\tan}$, for example, the outflow velocity (Swisdak & Drake, 2007) or reconnection rate (Borovsky, 2013), could provide a more likely explanation for the shift of the X line location in these simulations.

Using 3 years of Cluster observations, Wang et al. (2006) investigated the influence of solar wind parameters, including different components of the IMF, on FTE properties. The IMF B_z was found to be an important driver for almost all FTE attributes, but the authors also found some dependencies on B_x. In particular, they

found that FTE occurrence rates depend on both these IMF components. Our results show that the IMF tilt (positive B_x) has an impact on properties of FTEs in both the Northern and Southern Hemispheres. The comparison of the occurrence rate at different latitudes in both simulations shows that the positive IMF B_x component increases the probability of encountering an FTE on the Northern Hemisphere and decreases it on the Southern Hemisphere compared to the purely southward IMF case. The total FTE occurrence rate is higher in Run A with purely southward IMF, that is, larger southward IMF component and $B_x = 0$. Statistics by Wang et al. (2006) show a peak in the occurrence around $B_z = -3$ nT and an increasing occurrence rate with increasing IMF B_x. However, our results suggest that the effect of the IMF B_x on the occurrence rate depends on where the observer is located. In the Northern Hemisphere the observer would see an increased occurrence rate and in the Southern Hemisphere a decreased rate compared to the case without the IMF B_x component.

Figure 5 suggests that FTEs evolve differently northward and southward of the main X line when it is located away from the subsolar point. There are many more small FTEs on the higher-latitude side of the X line, when the X line itself is not located at the equator. Events generated at higher latitude move in the same direction as the background magnetosheath flow and leave the dayside region quickly without growing to large sizes. Some of the events generated closer to the equator move opposite to the magnetosheath flow and have more time to grow through reconnection and coalescence to larger sizes. This explains, at least partly, the north-south asymmetry in the occurrence rate, size, and velocity distributions. Similar behavior for FTEs was reported by Ku and Sibeck (1998) who used a 2-D single X line MHD model. They showed that FTEs moving in the direction of the magnetosheath flow accelerate, reducing the duration over which they can be observed. The velocity of FTEs moving opposite to the magnetosheath flow decreases, causing the event duration to become longer.

In conclusion, tilting a southward IMF so that it has a sunward component results in a smaller magnitude of the tangential magnetic field with north-south asymmetries in the magnetosheath close to the magnetopause due to the different angles between the IMF and the bow shock normal. Because the tangential field is smaller, the dayside reconnection rate is smaller as well. In addition, the tilt in the IMF causes a north-south asymmetry in properties of FTEs, including occurrence rate, size, and velocity that are not present in the simulation with a purely southward IMF orientation. Our results suggest, as a consequence of rotating the IMF to have a positive B_x component, that the FTEs on the Northern Hemisphere occur more frequently, are smaller, and accelerate faster than FTEs on the Southern Hemisphere.

Appendix A: X and O Point Location Calculations

We locate reconnection X lines (points in 2-D) and O points (FTEs) using a standard approach in 2-D simulations. We calculate the magnetic flux function $\psi(\mathbf{r}, t)$

$$\psi(\mathbf{r}, t) = \left(\int_{\mathbf{r}_0}^{\mathbf{r}} \mathbf{B}(\mathbf{r}, t) \times \mathrm{d}\mathbf{l} \right)_y , \tag{A1}$$

where $\mathbf{B}$ is the vector magnetic field and $\mathrm{d}\mathbf{l}$ is a path from a reference point $\mathbf{r}_0$ to the position $\mathbf{r}$ in question. In our simulations, the reference point is the lower (negative z) right (positive x) corner of the computational domain, and the magnetic flux there evolves in time due to input from the solar wind at the boundary. Contours of constant ψ are magnetic field lines. At any given time, the local maxima of ψ are magnetic O points, which are enclosed by magnetic islands, and the reconnecting X lines are saddle points in ψ (e.g., Servidio et al., 2009; Yeates & Hornig, 2011). The local maxima and saddles occur at points where $\nabla\psi = 0$, which are identified as points where the $\partial\psi/\partial x = 0$ and $\partial\psi/\partial z = 0$ contours cross each other. After identifying the points where $\nabla\psi = 0$, the type of the point is determined using the Hessian matrix H, whose determinant is $\det(H(x,z)) = \left(\partial^2\psi/\partial x^2\right)\left(\partial^2\psi/\partial z^2\right) - \left(\partial^2\psi/\partial x\partial z\right)^2$. If $\det(H(x,z)) < 0$, the point is a saddle point, whereas if $\det(H(x,z)) > 0$ and $\partial^2\psi/\partial x^2 < 0$, the point is a local maximum. Before finding the Hessian, we smooth ψ using a 2-D convolution over a five-cell box kernel.

Appendix B: Enclosed FTE Area

To calculate the enclosed area of FTEs, the previously determined X points on the magnetopause boundary are sorted according to their flux value (the X point with the highest flux value has already reconnected the

highest amount of flux). The magnetopause boundary is then recursively bisected into intervals delimited by the two X points with the highest flux value. Each of these intervals is assumed to contain one FTE, with the lower of the two X points' flux value identifying the enclosing magnetic field line contour. Using a flood-fill algorithm, starting from the previously determined O point locations as seed points, neighboring simulation cells are counted as belonging to the FTE if their flux value lies between the O point value and the flux value of the X point that closes the FTE contour. As a result, we obtain measures of FTE area.

Acknowledgments
We acknowledge the European Research Council for Starting grant 200141-QuESpace, with which Vlasiator (http://www.helsinki.fi/vlasiator) was developed, and Consolidator grant 682068-PRESTISSIMO awarded to further develop Vlasiator and use it for scientific investigations. This paper was outlined and drafted in the First International Vlasiator Science Hackathon held in Helsinki, 7–11 August 2017. The Hackathon was funded by the European Research Council grant 682068-PRESTISSIMO. We gratefully also acknowledge the Academy of Finland (grants 267144, 267186, and 309937). The Finnish Centre of Excellence in Research of Sustainable Space, funded through the Academy of Finland grant 312351, supports Vlasiator development and science as well. We acknowledge all computational grants we have received PRACE/Tier-0 2014112573 on HazelHen/HLRS, CSC-IT Center of Science Grand Challenge grant in 2016. We thank Rami Vainio for fruitful discussions and for applying for the computational grant with which the simulation used in this paper was produced. The work of S. H. at L. A. S. P. was supported by NASA MMS and THEMIS Missions. Work at NASA/GSFC was supported by the THEMIS Mission. P. A. C. gratefully acknowledges support from NASA grants NNX16AF75G and NNX16AG76G and NSF grant AGS-1602769. R. C. F. was supported by the U.K.'s Science and Technology Facilities Council (STFC) Ernest Rutherford FellowshipST/K004298/2. The work of L. T. was supported by a Marie Skłodowska-Curie Individual Fellowship (704681). Data used in this paper can be accessed by following the data policy on our web page (http://www.helsinki.fi/en/researchgroups/vlasiator/rules-of-the-road).

References

Akasofu, S.-I. (1981). Energy coupling between the solar wind and the magnetosphere. *Space Science Reviews*, *28*, 121–190. https://doi.org/10.1007/BF00218810

Akhavan-Tafti, M., Slavin, J. A., Le, G., Eastwood, J. P., Strangeway, R. J., Russell, C. T., et al. (2018). MMS examination of FTEs at the Earth's subsolar magnetopause. *Journal of Geophysical Research: Space Physics*, *123*, 1224–1241. https://doi.org/10.1002/2017JA024681

Angelopoulos, V. (2008). The THEMIS mission. *Space Science Reviews*, *141*(1), 5. https://doi.org/10.1007/s11214-008-9336-1

Baker, D. N., Pulkkinen, T. I., Angelopoulos, V., Baumjohann, W., & McPherron, R. L. (1996). Neutral line model of substorms: Past results and present view. *Journal of Geophysical Research*, *101*(A6), 12,975–13,010. https://doi.org/10.1029/95JA03753

Berchem, J., & Russell, C. T. (1984). Flux transfer events on the magnetopause: Spatial distribution and controlling factors. *Journal of Geophysical Research*, *89*(A8), 6689–6703. https://doi.org/10.1029/JA089iA08p06689

Blanco-Cano, X., Battarbee, M., Turc, L., Dimmock, A. P., Kilpua, E. K. J., Hoilijoki, S., et al. (2018). Cavitons and spontaneous hot flow anomalies in a hybrid-Vlasov global magnetospheric simulation. *Annales Geophysicae Discussions*, *2018*, 1–27. https://doi.org/10.5194/angeo-2018-22

Borovsky, J. E. (2013). Physical improvements to the solar wind reconnection control function for the Earth's magnetosphere. *Journal of Geophysical Research: Space Physics*, *118*, 2113–2121. https://doi.org/10.1002/jgra.50110

Burch, J. L., Moore, T. E., Torbert, R. B., & Giles, B. L. (2016). Magnetospheric multiscale overview and science objectives. *Space Science Reviews*, *199*(1), 5–21. https://doi.org/10.1007/s11214-015-0164-9

Burton, R. K., McPherron, R. L., & Russell, C. T. (1975). An empirical relationship between interplanetary conditions and Dst. *Journal of Geophysical Research*, *80*(31), 4204–4214. https://doi.org/10.1029/JA080i031p04204

Cassak, P. A., & Shay, M. A. (2007). Scaling of asymmetric magnetic reconnection: General theory and collisional simulations. *Physics of Plasmas*, *14*(10), 102114. https://doi.org/10.1063/1.2795630

Chapman, J. F., & Cairns, I. H. (2003). Three-dimensional modeling of Earth's bow shock: Shock shape as a function of Alfvén Mach number. *Journal of Geophysical Research*, *108*(A5), 1174. https://doi.org/10.1029/2002JA009569

Daldorff, L. K., Tóth, G., Gombosi, T. I., Lapenta, G., Amaya, J., Markidis, S., & Brackbill, J. U. (2014). Two-way coupling of a global Hall magnetohydrodynamics model with a local implicit particle-in-cell model. *Journal of Computational Physics*, *268*, 236–254. https://doi.org/https://doi.org/10.1016/j.jcp.2014.03.009

Dong, X.-C., Dunlop, M. W., Trattner, K. J., Phan, T. D., Fu, H.-S., Cao, J.-B., et al. (2017). Structure and evolution of flux transfer events near dayside magnetic reconnection dissipation region: MMS observations. *Geophysical Research Letters*, *44*, 5951–5959. https://doi.org/10.1002/2017GL073411

Dungey, J. W. (1961). Interplanetary magnetic field and the auroral zones. *Physical Review Letters*, *6*, 47–48. https://doi.org/10.1103/PhysRevLett.6.47

Eastwood, J. P., Phan, T. D., Cassak, P. A., Gershman, D. J., Haggerty, C., Malakit, K., & Wang, S. (2016). Ion-scale secondary flux ropes generated by magnetopause reconnection as resolved by MMS. *Geophysical Research Letters*, *43*, 4716–4724. https://doi.org/10.1002/2016GL068747

Fear, R. C., Milan, S. E., Fazakerley, A. N., Lucek, E. A., Cowley, S. W. H., & Dandouras, I. (2008). The azimuthal extent of three flux transfer events. *Annales Geophysicae*, *26*, 2353–2369. https://doi.org/10.5194/angeo-26-2353-2008

Fear, R. C., Milan, S. E., Fazakerley, A. N., Owen, C. J., Asikainen, T., Taylor, M. G. G. T., et al. (2007). Motion of flux transfer events: A test of the Cooling model. *Annales Geophysicae*, *25*(7), 1669–1690. https://doi.org/10.5194/angeo-25-1669-2007

Fear, R. C., Palmroth, M., & Milan, S. E. (2012). Seasonal and clock angle control of the location of flux transfer event signatures at the magnetopause. *Journal of Geophysical Research*, *117*, A04202. https://doi.org/10.1029/2011JA017235

Fedder, J. A., Slinker, S. P., Lyon, J. G., & Russell, C. T. (2002). Flux transfer events in global numerical simulations of the magnetosphere. *Journal of Geophysical Research*, *107*(A5), 1048. https://doi.org/10.1029/2001JA000025

Fermo, R. L., Drake, J. F., Swisdak, M., & Hwang, K.-J. (2011). Comparison of a statistical model for magnetic islands in large current layers with Hall MHD simulations and Cluster FTE observations. *Journal of Geophysical Research*, *116*, A09226. https://doi.org/10.1029/2010JA016271

Finn, J. M., & Kaw, P. K. (1977). Coalescence instability of magnetic islands. *The Physics of Fluids*, *20*(1), 72–78. https://doi.org/10.1063/1.861709

Hoilijoki, S., Ganse, U., Pfau-Kempf, Y., Cassak, P. A., Walsh, B. M., Hietala, H., et al. (2017). Reconnection rates and X line motion at the magnetopause: Global 2D-3V hybrid-Vlasov simulation results. *Journal of Geophysical Research: Space Physics*, *122*, 2877–2888. https://doi.org/10.1002/2016JA023709

Hoilijoki, S., Palmroth, M., Walsh, B. M., Pfau-Kempf, Y., von Alfthan, S., Ganse, U., et al. (2016). Mirror modes in the Earth's magnetosheath: Results from a global hybrid-Vlasov simulation. *Journal of Geophysical Research: Space Physics*, *121*, 4191–4204. https://doi.org/10.1002/2015JA022026

Hoilijoki, S., Souza, V. M., Walsh, B. M., Janhunen, P., & Palmroth, M. (2014). Magnetopause reconnection and energy conversion as influenced by the dipole tilt and the IMF B_x. *Journal of Geophysical Research: Space Physics*, *119*, 4484–4494. https://doi.org/10.1002/2013JA019693

Hoshi, Y., Hasegawa, H., Kitamura, N., Saito, Y., & Angelopoulos, V. (2018). Seasonal and solar wind control of the reconnection line location on the Earth's dayside magnetopause. *Journal of Geophysical Research: Space Physics*, *123*, 7498–7512. https://doi.org/10.1029/2018JA025305

Jarvinen, R., Vainio, R., Palmroth, M., Juusola, L., Hoilijoki, S., Pfau-Kempf, Y., et al. (2018). Ion acceleration by flux transfer events in the terrestrial magnetosheath. *Geophysical Research Letters*, *45*, 1723–1731. https://doi.org/10.1002/2017GL076192

Jeřáb, M., Němeček, Z., Šafránková, J., Jelínek, K., & Měrka, J. (2005). Improved bow shock model with dependence on the IMF strength. *Planetary and Space Science*, *53*, 85–93. https://doi.org/10.1016/j.pss.2004.09.032

Juusola, L., Hoilijoki, S., Pfau-Kempf, Y., Ganse, U., Jarvinen, R., Battarbee, M., et al. (2018). Fast plasma sheet flows and X line motion in the Earth's magnetotail: Results from a global hybrid-Vlasov simulation. *Annales Geophysicae*, *36*(5), 1183–1199. https://doi.org/10.5194/angeo-36-1183-2018

Karlson, K. A., Øieroset, M., Moen, J., & Sandholt, P. E. (1996). A statistical study of flux transfer event signatures in the dayside aurora: The IMF By -related prenoon-postnoon symmetry. *Journal of Geophysical Research*, *101*(A1), 59–68. https://doi.org/10.1029/95JA02590

Kawano, H., & Russell, C. T. (1997). Survey of flux transfer events observed with the ISEE 1 spacecraft: Dependence on the interplanetary magnetic field. *Journal of Geophysical Research*, *102*(A6), 11,307–11,313. https://doi.org/10.1029/97JA00481

Kempf, Y., Pokhotelov, D., Gutynska, O., Wilson III, L. B., Walsh, B. M., von Alfthan, S., et al. (2015). Ion distributions in the Earth's foreshock: Hybrid-Vlasov simulation and THEMIS observations. *Journal of Geophysical Research: Space Physics*, *120*, 3684–3701. https://doi.org/10.1002/2014JA020519

Ku, H. C., & Sibeck, D. G. (1998). The effect of magnetosheath plasma flow on flux transfer events produced by the onset of merging at a single X line. *Journal of Geophysical Research*, *103*(A4), 6693–6702. https://doi.org/10.1029/97JA03688

Lee, L. C., & Fu, Z. F. (1985). A theory of magnetic flux transfer at the Earth's magnetopause. *Geophysical Research Letters*, *12*, 105–108. https://doi.org/10.1029/GL012i002p00105

Lin, Y., Swift, D. W., & Lee, L. C. (1996). Simulation of pressure pulses in the bow shock and magnetosheath driven by variations in interplanetary magnetic field direction. *Journal of Geophysical Research*, *101*(A12), 27,251–27,269. https://doi.org/10.1029/96JA02733

McPherron, R. L., Terasawa, T., & Nishida, A. (1986). Solar wind triggering of substorm expansion onset. *Journal of geomagnetism and geoelectricity*, *38*(11), 1089–1108. https://doi.org/10.5636/jgg.38.1089

Merka, J., Szabo, A., Slavin, J. A., & Peredo, M. (2005). Three-dimensional position and shape of the bow shock and their variation with upstream Mach numbers and interplanetary magnetic field orientation. *Journal of Geophysical Research*, *110*, A04202. https://doi.org/10.1029/2004JA010944

Omidi, N., Blanco-Cano, X., Russell, C., & Karimabadi, H. (2006). Global hybrid simulations of solar wind interaction with Mercury: Magnetosperic boundaries. *Advances in Space Research*, *38*(4), 632–638. Mercury, Mars and Saturn https://doi.org/https://doi.org/10.1016/j.asr.2005.11.019

Palmroth, M., Archer, M., Vainio, R., Hietala, H., Pfau-Kempf, Y., Hoilijoki, S., et al. (2015). ULF foreshock under radial IMF: THEMIS observations and global kinetic simulation Vlasiator results compared. *Journal of Geophysical Research: Space Physics*, *120*, 8782–8798. https://doi.org/10.1002/2015JA021526

Palmroth, M., Ganse, U., Pfau-Kempf, Y., Battarbee, M., Turc, L., Brito, T., et al. (2018). Vlasov methods in space physics and astrophysics. *Living Reviews in Computational Astrophysics*, *4*(1), 1. https://doi.org/10.1007/s41115-018-0003-2

Palmroth, M., Hietala, H., Plaschke, F., Archer, M., Karlsson, T., Blanco-Cano, X., et al. (2018). Magnetosheath jet properties and evolution as determined by a global hybrid-Vlasov simulation. *Annales Geophysicae*, *36*(5), 1171–1182. https://doi.org/10.5194/angeo-36-1171-2018

Palmroth, M., Hoilijoki, S., Juusola, L., Pulkkinen, T. I., Hietala, H., Pfau-Kempf, Y., et al. (2017). Tail reconnection in the global magnetospheric context: Vlasiator first results. *Annales Geophysicae*, *35*(6), 1269–1274. https://doi.org/10.5194/angeo-35-1269-2017

Peng, Z., Wang, C., & Hu, Y. Q. (2010). Role of IMF Bx in the solar wind-magnetosphere-ionosphere coupling. *Journal of Geophysical Research*, *115*, A08224. https://doi.org/10.1029/2010JA015454

Pfau-Kempf, Y., Hietala, H., Milan, S. E., Juusola, L., Hoilijoki, S., Ganse, U., et al. (2016). Evidence for transient, local ion foreshocks caused by dayside magnetopause reconnection. *Annales Geophysicae*, *34*(11), 943–959. https://doi.org/10.5194/angeo-34-943-2016

Rijnbeek, R. P., Cowley, S. W. H., Southwood, D. J., & Russell, C. T. (1984). A survey of dayside flux transfer events observed by ISEE 1 and 2 magnetometers. *Journal of Geophysical Research*, *89*(A2), 786–800. https://doi.org/10.1029/JA089iA02p00786

Russell, C. T., & Elphic, R. C. (1978). Initial ISEE magnetometer results—Magnetopause observations. *Space Science Reviews*, *22*, 681–715. https://doi.org/10.1007/BF00212619

Servidio, S., Matthaeus, W. H., Shay, M. A., Cassak, P. A., & Dmitruk, P. (2009). Magnetic reconnection in two-dimensional magnetohydrodynamic turbulence. *Physical Review Letters*, *102*, 115003. https://doi.org/10.1103/PhysRevLett.102.115003

Southwood, D., Farrugia, C., & Saunders, M. (1988). What are flux transfer events?. *Planetary and Space Science*, *36*(5), 503–508. https://doi.org/10.1016/0032-0633(88)90109-2

Swisdak, M., & Drake, J. F. (2007). Orientation of the reconnection X-line. *Geophysical Research Letters*, *34*, L11106. https://doi.org/10.1029/2007GL029815

Trattner, K. J., Mulcock, J. S., Petrinec, S. M., & Fuselier, S. A. (2007). Probing the boundary between antiparallel and component reconnection during southward interplanetary magnetic field conditions. *Journal of Geophysical Research*, *112*, A08210. https://doi.org/10.1029/2007JA012270

Trattner, K. J., Petrinec, S. M., Fuselier, S. A., & Phan, T. D. (2012). The location of reconnection at the magnetopause: Testing the maximum magnetic shear model with THEMIS observations. *Journal of Geophysical Research*, *117*, A01201. https://doi.org/10.1029/2011JA016959

Treumann, R. A. (2009). Fundamentals of collisionless shocks for astrophysical application, 1. Non-relativistic shocks. *The Astronomy and Astrophysics Review*, *4*, 409–535. https://doi.org/10.1007/s00159-009-0024-2

Turc, L., Fontaine, D., Escoubet, C. P., Kilpua, E. K. J., & Dimmock, A. P. (2017). Statistical study of the alteration of the magnetic structure of magnetic clouds in the Earth's magnetosheath. *Journal of Geophysical Research: Space Physics*, *122*, 2956–2972. https://doi.org/10.1002/2016JA023654

Turc, L., Fontaine, D., Savoini, P., & Kilpua, E. K. J. (2014). A model of the magnetosheath magnetic field during magnetic clouds. *Annales Geophysicae*, *32*, 157–173. https://doi.org/10.5194/angeo-32-157-2014

Turc, L., Fontaine, D., Savoini, P., & Modolo, R. (2015). 3D hybrid simulations of the interaction of a magnetic cloud with a bow shock. *Journal of Geophysical Research: Space Physics*, *120*, 6133–6151. https://doi.org/10.1002/2015JA021318

Turc, L., Ganse, U., Pfau-Kempf, Y., Hoilijoki, S., Battarbee, M., Juusola, L., et al. (2018). Foreshock properties at typical and enhanced interplanetary magnetic field strengths: Results from hybrid-Vlasov simulations. *Journal of Geophysical Research: Space Physics*, *123*, 5476–5493. https://doi.org/10.1029/2018JA025466

Vasyliunas, V. M. (1975). Theoretical models of magnetic field line merging. *Reviews of Geophysics*, *13*(1), 303–336. https://doi.org/10.1029/RG013i001p00303

von Alfthan, S., Pokhotelov, D., Kempf, Y., Hoilijoki, S., Honkonen, I., Sandroos, A., & Palmroth, M. (2014). Vlasiator: First global hybrid-Vlasov simulations of Earth's foreshock and magnetosheath. *Journal of Atmospheric and Solar-Terrestrial Physics*, *120*, 24–35. https://doi.org/10.1016/j.jastp.2014.08.012

Wang, Y. L., Elphic, R. C., Lavraud, B., Taylor, M. G. G. T., Birn, J., Raeder, J., et al. (2005). Initial results of high-latitude magnetopause and low-latitude flank flux transfer events from 3 years of Cluster observations. *Journal of Geophysical Research*, *110*, A11221. https://doi.org/10.1029/2005JA011150

Wang, Y. L., Elphic, R. C., Lavraud, B., Taylor, M. G. G. T., Birn, J., Russell, C. T., et al. (2006). Dependence of flux transfer events on solar wind conditions from 3 years of Cluster observations. *Journal of Geophysical Research*, *111*, A04224. https://doi.org/10.1029/2005JA011342

Yeates, A. R., & Hornig, G. (2011). A generalized flux function for three-dimensional magnetic reconnection. *Physics of Plasmas*, *18*, 102118. https://doi.org/10.1063/1.3657424

Zhong, Z. H., Tang, R. X., Zhou, M., Deng, X. H., Pang, Y., Paterson, W. R., et al. (2018). Evidence for secondary flux rope generated by the electron Kelvin-Helmholtz instability in a magnetic reconnection diffusion region. *Physical Review Letters*, *120*, 75101. https://doi.org/10.1103/PhysRevLett.120.075101